AN OBJECT-ORIENTED CLASSIFICATION OF IMPACT CRATERS USING LUNAR RECONNAISSANCE ORBITER DATA

A thesis submitted to the faculty of
San Francisco State University
In partial fulfillment of
the requirements for
the Degree

Master of Science

In

Geographic Information Science

by

Allison Haley Barnes

San Francisco, California

January 2016

CERTIFICATION OF APPROVAL

I certify that I have read An Object-Oriented Classification of Impact Craters Using Lunar Reconnaissance Orbiter Data by Allison Haley Barnes, and that in my opinion this work meets the criteria for approving a thesis submitted in partial fulfillment of the requirement for the degree Master of Science in Geographic Information Science at San Francisco State University.

Leonhard Blesius, Ph.D.
Associate Professor of Geography

Jerry Davis, Ph.D.
Professor of Geography

AN OBJECT-ORIENTED CLASSIFICATION OF IMPACT CRATERS USING LUNAR RECONNAISSANCE ORBITER DATA

Allison Haley Barnes
San Francisco, California
2016

Object-based image analysis is used to perform crater detection. High-resolution Lunar Reconnaissance Orbiter Narrow Angle Camera images are used with a resolution of one meter per pixel. This CDA detects craters ranging from one meter to one kilometer in radius. The algorithm is implemented in eCognition, ArcMap, and Python, using segmentation and object-oriented classification procedures iterating over the scale parameter and focusing on different levels of brightness. The segmentation uses high values for the shape and compactness parameters, resulting in a preference for the nearly circular shapes associated with impact craters. A three-tiered classification scheme is used which takes advantage of paired patterns of light and shadow. Although many areas in the image are determined to be illuminated or shadowed, the pairing process filters out those most likely to be craters. A quality rate of 60.11%, true detection rate of 68.88%, and false detection rate of 17.48% are achieved.

I certify that the Abstract is a correct representation of the content of this thesis.

_____ _____

Chair, Thesis Committee Date

TABLE OF CONTENTS

LIST OF TABLES

Tables Page

LIST OF FIGURES

Figures Page

1. Introduction

The objective of this research is to detect impact craters on the Moon from Lunar Reconnaissance Orbiter (LRO) data using object-based image analysis (OBIA). Many methods have been employed to automatically detect impact craters. Although OBIA is increasingly used in terrestrial remote sensing applications, it is quite underrepresented in the crater detection algorithm (CDA) literature. Therefore, this research presents a unique opportunity to explore the applicability of OBIA to crater detection.

The Earth remains the primary focus of remote sensing. However, data collection is not limited to Earth. Many extraterrestrial bodies, such as the Moon and Mars, are subject to an increasing amount of scientific inquiry. As the number of missions exploring the Solar System continues to grow, the volume of data returned from these missions has grown astronomically, such that manual data analysis is no longer feasible (1, 10, 9, 40, 7). If limited to manual analysis, the remote sensing community would only be able to utilize a minute proportion of the available data (10). As a result, the development of automatic procedures for analyzing such data is crucial (35, 10, 9, 40, 7). Mission-acquired data can include panchromatic, multispectral, or hyperspectral imagery, laser altimetry, and synthetic aperture radar (28, 6). The analysis of mission-acquired data involves the transformation of raw data into knowledge, usually in the form of a thematic map (10). This is achieved through classification, which constitutes a significant field of study within lunar and planetary science (28). Closely related is the detection of a particular feature of interest, which includes both recognition in the form of localization and dimensionality and classification as either feature of interest or non-feature of interest (1, 20).

Collisions between meteoroids, asteroids, or comets with lunar or planetary surfaces occur despite the astronomical distances that characterize the Solar System (8, 3). These collisions create impact craters, which are concave bowl-shaped topographic depressions (42, 1, 37, 8, 2, 17). Craters can be classified, from smallest to largest, as microcraters/pits, small/simple craters, large/complex craters, and multiring basins (42,

28, 8, 31, 40). Microcraters/pits, which are sub-centimeter in scale, are formed by impacts of micrometeoroids or cosmic dust grains (8). Small/simple craters, which tend to have diameters up to several kilometers, display the well-known bowl shape and represent the most common type of observed craters (42, 1, 8, 2, 30, 40, 7). In imagery, these craters tend to display a characteristic pair of highlight and shadow crescents, resulting from the angle of solar illumination, elevated rims, and inner depression (42, 1, 38, 2). Large/complex craters, which tend to have diameters of tens to hundreds of kilometers, display flat floors, central peaks, and terraced rims (42, 35, 8, 2, 30, 7). Multiring basins, which are significantly larger than large/complex craters, display concentric rings (42, 8, 30).

Crater density, quantity, distribution, morphology, and degradation often present the only viable method for remote estimation of surface age. Craters also reveal information about historical impact rate, surface geology, stratigraphy, weathering, and other processes (15, 35, 1, 26, 27, 22, 37, 38, 11, 28, 6, 8, 9, 13, 2, 31, 23, 40, 7, 12, 32). Each of these investigations requires large amounts of data, and thus the manual detection of craters proves impractical (35, 1, 38, 9, 2, 23, 12). Therefore, automation is needed to achieve statistically meaningful results (38, 26, 9, 2). Due to their relative abundance, small craters are natural targets for such approaches, and the automation of their detection is the focus of this study.

Automated CDAs are a subject of intensive study within lunar and planetary science, but research has faced a variety of challenges (35, 1, 38, 23, 7, 32, 28, 9, 29). The range of observed crater sizes spans multiple orders of magnitude, so CDAs must be capable of analyzing imagery or DEMs at multiple scales (4, 20, 9, 2). Additionally, crater morphology increases in complexity with increasing diameter (42, 35). Rims, the most prominent features of craters, experience erosion (42). Therefore, CDAs must be capable of detecting crater rims ranging from fresh and sharp to old and blurry (42, 20, 11, 28, 9, 2, 31, 40, 7, 12). Craters frequently overlap, which increases the analytical demand on CDAs (11, 9, 2). Lunar and planetary surfaces

display heterogeneous morphology, which further complicates the separation of craters from their background (9, 40, 12). Imagery is obtained at varying spatial resolution and under varying solar illumination, which can result in the same crater appearing differently in separate images (42, 20, 9, 2, 40, 12). Creating a CDA capable of serving all applications is complicated by the varying quality that each necessitates (29).

No currently existing CDA is capable of generating results of sufficient quality to be utilized for all applications on all lunar or planetary surfaces (1, 20, 2, 30). Despite the wide range of techniques, all CDAs inherently rely on pattern recognition and some form of classification (7). As of 2014, 140 CDA articles had been published. Of these 140 articles, 59% are imagery-based; 28% are DEM-based; 11% are both imagery- and DEM-based; and 2% are based on other data types (31, 32). Edge detection, Hough transform, and machine learning represent the most common techniques utilized in CDAs (31). The following paragraphs will discuss a technique rarely applied to CDAs in more detail, because it will be used in this research.

The last decade and a half witnessed the development of satellite systems capable of producing very high-resolution imagery (39), with spatial resolutions less than or equal to one meter (33). While pixel-based classification is effective on small- and medium-resolution imagery, it is less effective on high-resolution imagery (10, 14, 39, 19, 33, 45), which presents an overabundance of details. This increases intra-class and decreases inter-class spectral heterogeneity and reduces the utility of spectral information to independently distinguish among classes, necessitating the additional use of ancillary data to perform effective classification (39, 5, 33, 24, 25). Whereas pixel-based classification only utilizes spectral characteristics of individual pixels, object-based classification utilizes various characteristics of individual objects (39, 33, 34, 24, 45). Performing image analysis with objects instead of pixels allows for the utilization of more data characteristics and more complicated procedures. Object-based image analysis allows the analyst to easily adjust parameters and repeat the analysis in order to optimize the result (39). Therefore, the recent technological advancement in satellite systems

instigated a transformation of the basic entity of image analysis from pixels to objects and an expansion of the generally utilized data beyond solely spectral information. Even though spectral information is the most frequently utilized data in image classification, the addition of ancillary data improves classification performance (5). Whereas pixel-based classification can produce results plagued by the salt-and-pepper effect, object-based classification can reduce the noise that frequently characterizes high spatial resolution data (33). The result of an object-based classification more closely resembles that of visual interpretation, mimicking the human recognition process (18, 39, 33, 34, 45).

The procedure of OBIA involves pre-processing, segmentation, object-based classification, post-classification, and accuracy assessment (14, 39, 24). Pre-processing can include radiometric, geometric, and atmospheric corrections, as well as registration, orthorectification, and lidar interpolation (39). Segmentation partitions the image into non-overlapping objects, or groups of spatially adjacent and homogeneous pixels, and determines the spectral, geometric, contextual, textural, conceptual, morphologic, and temporal attributes of the objects (14, 18, 39, 5, 3, 21, 24). Segmentation relies on certain parameters, including weight, scale, shape, and compactness. Since segmentation quality depends on parameter selection, some researchers use trial-and-error while others use machine learning to optimize these parameters. Object-based classification then groups the objects into classes based on these attributes (14, 39, 3, 24). Segmentation and object-based classification are closely related, in that the quality of the latter directly depends on the quality of the former (14, 39, 44). OBIA can produce results in the form of raster or vector data, specifically polygons, which allows for the utilization of GIS operations and simplifies post-processing (39, 33). Post-classification can involve manual confirmation of results and elimination of errors, field inspection, or reference source comparison, while accuracy assessment quantifies the quality of the result (39).

Table 1 presents the only four instances of object-based classification that have occurred in the CDA literature (4, 43, 10, 41). The first study utilizes a DEM derived

from data acquired by the Mars Orbiter Laser Altimeter on the Mars Global Surveyor spacecraft, which has an approximate resolution of 500 meters per pixel. This study achieves a quality rate of 61% and a true detection rate of 74% (4). The second study utilizes lunar imagery obtained by the Ultraviolet/Visible Camera on the Clementine satellite, which has an approximate resolution of 100 meters per pixel. Although this study does not report a quality rate or true detection rate, it validates its results through the use of a formula that determines surface age from the number of craters and then comparison of this formula-derived age with a reference age (43). The third study utilizes a DEM derived from data acquired by the Mars Orbiter Laser Altimeter on the Mars Global Surveyor spacecraft, which has an approximate resolution of 500 meters per pixel. This study achieves overall accuracies ranging from 40% to 90%, depending on the test area and classifier utilized (10). The fourth study utilizes a DEM derived from lunar data acquired by the CCD stereo camera on the Chang'E-1 satellite, which has an approximate resolution of 500 meters per pixel. This study achieves overall accuracies ranging from 65% to 78%, depending on the test area and classifier utilized (41).

Table 1: Literature Comparison. Instances and characteristics of OBIA in CDA literature.

	Location	**Data**	**Resolution**	**Accuracy**
Bue & Stepinski, 2007	Mars	DEM	500 meters/pixel	61 – 74%
Yue *et al.*, 2008	Moon	Imagery	100 meters/pixel	Not Reported
Ghosh *et al.*, 2010	Mars	DEM	500 meters/pixel	40 – 90%
Wan *et al.*, 2012	Moon	DEM	500 meters/pixel	65 – 78%

The resolution of the data utilized by the CDA determines the minimum crater size identified. While the resolution of the data utilized in the above four studies ranges from 100 to 500 meters per pixel, the resolution of the data utilized in this CDA is one meter per pixel. Whereas the minimum crater size detected by the above four studies is approximately one kilometer in radius, the minimum crater size detected by this CDA is approximately one meter in radius.

2. Study Area

The study area for this project is on the Moon. Although this CDA could be applied to any LROC NAC image, the area used for the accuracy assessment is a subset of the image with product name M114227172LC and is located at -11.1 degrees latitude and 318.4 degrees longitude. The area is 5.7 kilometers by 4.4 kilometers, which constitutes a total area of 25 square kilometers. This particular area was selected over other possible areas because it contains a wide range of crater sizes.

The lunar and planetary science community theorizes that the Moon was formed approximately 4.5 billion years ago as a result of a collision between a Mars-sized impactor and Earth. With a radius of approximately 1,737 kilometers, the Moon displays the following average values: albedo (0.113), crustal density (2.85 grams per cubic centimeter), surface temperature (277 Kelvin), and surface pressure ($3*10^{-15}$ bars). The Moon's atmosphere, which consists of helium, argon, sodium, and potassium, is so tenuous that it resembles a vacuum and was partially formed by the continual bombardment of impactors over billions of years. Although volcanism and tectonics acted on the Moon, most activity ceased approximately 3 billion years ago. The only active processes affecting the Moon are impact cratering and tidally- and thermally-induced moonquakes.

The lunar surface can be classified into two groups: the bright highlands (covering 80% of the surface) and the dark maria (covering 16% of the surface). The acquisition of 382 kilograms of lunar rock samples by the Apollo and Luna missions allowed scientists to determine absolute ages via radioisotope dating. While the highlands are approximately 4.4 billion years old, the maria are approximately 3.5 billion years old. The regolith, which was created by the continual bombardment of impactors over billions of years, is approximately fifteen meters deep in the highlands and approximately two to eight meters deep in the maria. The maria are younger than the highlands because they constitute subsurface material subsequently brought to the surface via volcanism. Although volcanic features (e.g., basins and mountains) and tectonic features (e.g.,

grabens and horsts) are visible on the surface, impact craters represent the most dominant feature on the surface (42, 11, 8).

The lunar surface is nearly saturated with craters; however, the highlands are more heavily cratered (8, 17). Considering that the highlands were determined to be significantly older via radioisotope dating (8), this evidence supports the theory that crater density and surface age display a direct relationship. The historic cratering rate can be determined from the radioisotope-dated samples and the crater size-frequency distribution (8). The historic cratering rate indicates that the Moon experienced two periods of heightened cratering rates, referred to as the early bombardment era (approximately 4.4 billion years ago) and the late heavy bombardment era (approximately 3.8 to 3.9 billion years ago) (11, 8). Lunar impact craters range in size from micrometers to hundreds of kilometers, with a transition size between simple and complex craters of approximately twelve kilometers (42, 8). Large craters tend to concentrate in the highlands, and small craters tend to concentrate in the maria (17).

3. Methods

3.1. Data

The data utilized in this project were acquired by the Lunar Reconnaissance Orbiter Camera (LROC) and are available to the public for free. The LRO spacecraft is currently in a polar orbit around the Moon at altitudes ranging from 50 to 200 kilometers. Its mission objectives include assessment of potential landing sites and the creation of accurate, high-resolution thematic maps, both of which are assisted by CDAs. LROC contains two Narrow Angle Cameras (NACs). They are narrow-angle push-broom imaging cameras that capture panchromatic imagery (400 to 750 nanometers) at an approximate resolution of 0.5 meters per pixel over a 5-kilometer swath (36, 16).

3.2. Pre-Processing

To transform the raw data into a format appropriate for use in the eCognition-based CDA, georeferencing and standardization are performed in ArcMap. Georeferencing applies a coordinate system to the data so that accuracy assessment can be reliably performed and output data can be used in other applications. Standardization is necessary to account for the variety of factors that can influence the appearance of the image. These include the differing reflectivity of varying soil types and the changing angle and intensity of the sun from image to image.

Images are georeferenced to the Geographic Coordinate System GCS_Moon_2000 with Datum D_Moon_2000 within ArcMap. The four vertices of the coverage shapefiles (which are already georeferenced to the specified coordinate system) are used as control points in the georeferencing process for the calibrated imagery. Once the four control points are generated, the image is rectified using nearest neighbor and a first-order polynomial transformation.

Due to the vast coverage of each LROC NAC image, a single image is determined sufficient to be the input for this CDA. Multiple images could be mosaicked together, and the algorithm applied to the result. However, this would introduce additional complexity and could obscure the results of the novel methods.

Standardization of the data is performed so that the inputs to the CDA are consistent regardless of the source image. Therefore, identical classification thresholds can be used. The standardization step operates under the assumption that the radiance values of the LROC NAC images follow a normal distribution. This step transforms the normal distribution into a standardized normal distribution with a mean of 0 and a standard deviation of 100 by using Map Algebra. These values are used instead of the standard normal, mean of 0 and standard deviation of 1, because the eCognition segmentation algorithm functions differently for different standard deviations.

3.3. Crater Detection Algorithm

The small/simple crater class is distinguished from non-craters in an image by a distinctive pattern of dark and light crescents. Figure 1a shows an example of a small crater featuring this pattern. These crescents occur from oblique illumination by the sun across a well-defined crater ridge. The side of the crater further from the sun is illuminated more brightly than the surrounding soil due to a more direct angle, while the other side sits in the shadow. This specific brightness profile can be exploited by object-based image analysis for crater detection.

Segmentation is applied to the image in eCognition. This splits the image into a collection of objects, the borders of which delineate different clusters of pixels with similar properties. In this instance, the standardized brightness is used as the defining property. Shape and compactness parameters, which in eCognition denote the preference for roundness over homogeneity of segments, are both set to maximum since the shapes this CDA aims to detect are near circular. This includes craters resulting from oblique impacts, which are somewhat elliptical. Because the segmentation process relies on a relative weighting scheme between shape and homogeneity, it is robust to these irregularities, and such craters do not pose an issue. The scale parameter can vary the average size of these segments, which can adjust the result to be more appropriate for different sizes of craters. To make the CDA applicable to a large range of crater sizes, iteration is performed over different values of this parameter. Because of the rotational symmetry of segmentation in eCognition, this CDA is independent of solar illumination angle. However, because of this symmetry a near circular peak can theoretically be detected as a crater in this CDA. Such features are relatively rare on the Moon, and the study area did not include them, but this could be a source of error in other areas. Figure 1b shows the result of segmentation at a single scale on the example area.

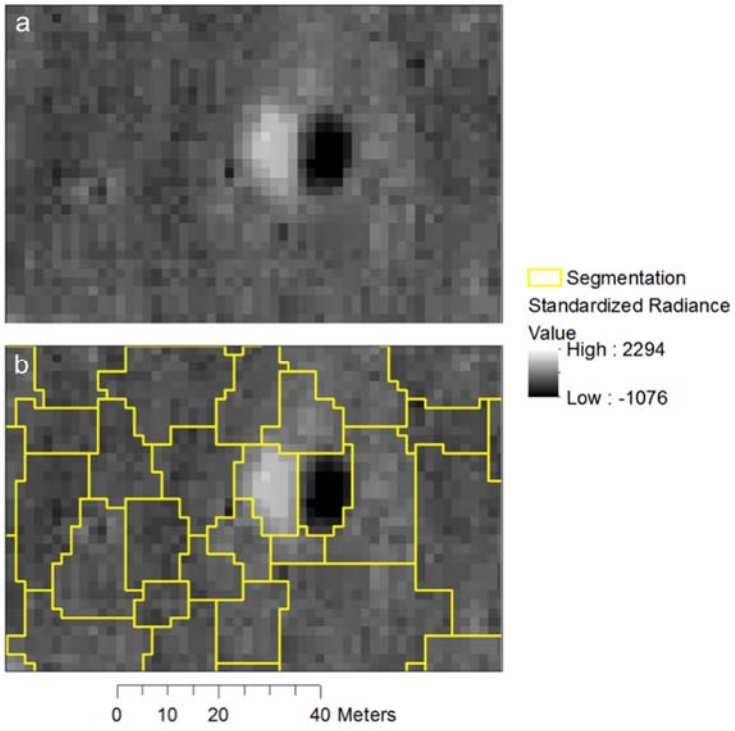

Figure 1: Segmentation. A crater is taken through the processing steps in order to demonstrate the detection process in eCognition.
(a) One crater is visible and surrounded by noise.
(b) The area from (a) is segmented, with each side of the crater constituting one segment.

For every segmentation, each of which corresponds to a particular scale parameter, a three-step classification scheme determines which segments depict a crater. On the first level of classification, segments are catalogued as Light, Medium, or Dark. Medium encompasses objects with standardized brightness values within one standard deviation from the mean. Light and Dark denote objects with standardized brightness values at least one standard deviation greater than or less than the mean, respectively. Figure 2a shows the example area classified at level one. The actual crater is identified as Light and Dark, but there are also Dark regions that do not correspond to craters.

Light or Dark segments are further analyzed in level two. If a Light segment is within a specified distance from a Dark segment, then that segment is labeled as Light Crater. An analogous process classifies Dark Crater. This parity of Light and Dark segments is the key distinguishing characteristic of a crater and lends the CDA much of its efficacy. Figure 2b shows the example area classified in level two. The non-crater Dark segments of level one have been eliminated, as they are too distant from the Light segment. However, the crater remains classified as two separate classes.

In the classification of level three, Light Crater and Dark Crater segments are combined into Crater, while all other segments are combined into No Crater. Table 2 shows the rules used in eCognition to define these classes. Figure 2c shows the example area classified in level three. The crater is effectively identified and unified.

Table 2: Class Description.

Class	Level	Description
Light	1	Mean Radiance > 100
Medium	1	Mean Radiance ≤ 100 AND Mean Radiance ≥ -100
Dark	1	Mean Radiance < -100
Light Crater	2	Classified as Light = 1 AND (Distance to Dark Crater < D OR Distance to Dark < D)
Dark Crater	2	Classified as Dark = 1 AND (Distance to Light Crater < D OR Distance to Light < D)
Crater	3	Classified as Light Crater = 1 OR Classified as Dark Crater = 1
No Crater	3	Classified as Crater = 0

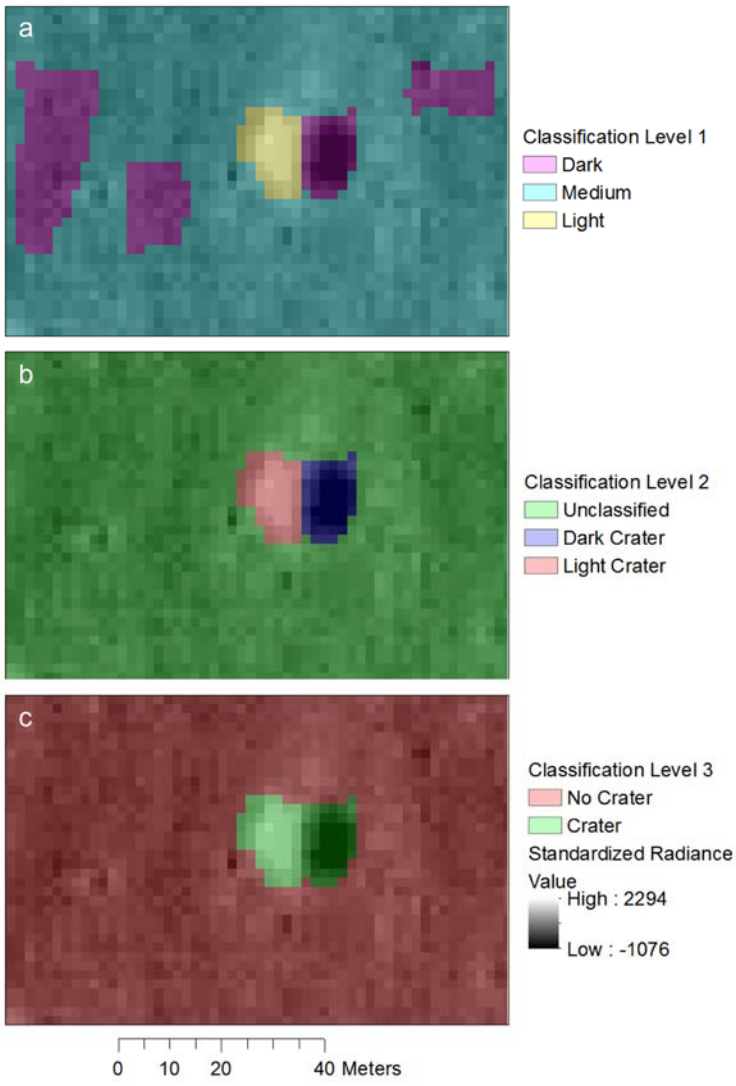

Figure 2: Classification at Level One, Two, and Three.

(a) Level 1. The crater is classified as Dark or Light, while most of the area is classified as Medium. However, there are areas classified as Dark that are not craters.

(b) Level 2. The light and dark sides of the crater are classified as Light Crater and Dark Crater, respectively. The segments previously classified as Dark are now Unclassified, due to the distance scaling (Table 3).

(c) Level 3. The final classification result for the example crater. Segments classified as No Crater or Crater are merged to produce this final result.

At level two, a particular distance is used as a threshold. This value determines how close Light and Dark segments need to be to each other in order to be classified as Light Crater or Dark Crater. In eCognition, the distance between two objects is a centroid distance. Since iteration is performed over the scale parameter, the distance between adjacent objects will vary throughout the process. Therefore, this threshold distance needs to vary along with the scale parameter throughout the iteration. The distances between segments constituting actual craters of various sizes are measured manually. Appropriate threshold values are determined to maximize true positives while minimizing false negatives. Table 3 shows the value pairs used.

Table 3: Distance Scaling. Distance between segments at each scale parameter.

Scale Parameter	Distance (pixels)
10	10
20 – 30	20
40 – 80	30
90 – 190	50
200 – 230	60
240 – 290	250
300 – 390	350
400 – 490	400
500 – 1000	500

The OBIA algorithm in eCognition is shown in Figure 3. Using this algorithm, eCognition produces one output map for each scale parameter. These maps are each exported as color-coded TIFF files. Then, a python script performs a weighted overlay process in ArcMap combining the 100 layers into a single result. Different weights are used for outputs produced using different scale parameters due to the relative importance of small craters, which are only detected with lower scale parameters. These weights are manually optimized in order to produce similar crater detection performance over the whole range of crater sizes this CDA aims to detect. Table 4 shows the weights used for each scale parameter.

Table 4: Scale Coefficient. Coefficient assigned to the result of each scale parameter in weighted overlay process.

Scale Parameter	Coefficient
10 – 100	64
110 – 300	16
310 – 600	4
610 – 1000	1

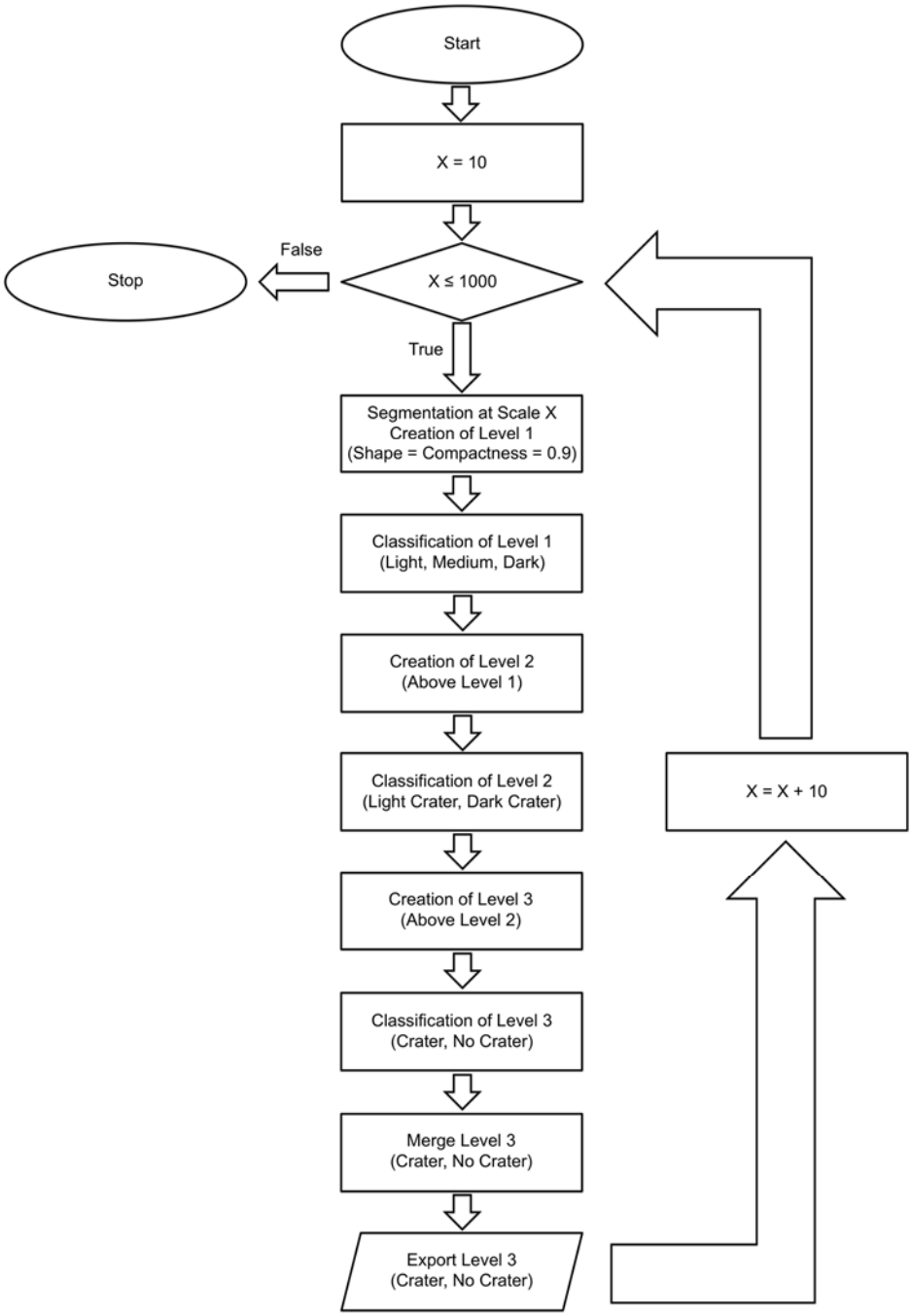

Figure 3: Algorithm Schematic. The steps taken in eCognition to produce 100 classification results that are later input into the weighted overlay process.

The final result of this algorithm is a single raster map, which assigns a value to each pixel corresponding to the likelihood that pixel is part of a crater. Figures 4 and 5 show these results at differing levels of zoom. Figure 5 is the full output of the algorithm on the entire study area and is the foundation of the accuracy assessment to follow.

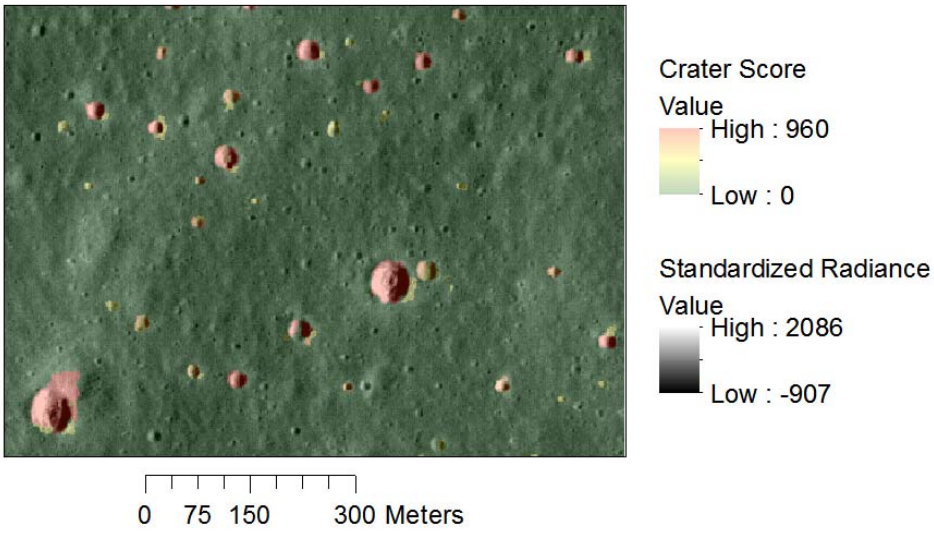

Figure 4: Selected Results. While Figure 2c presents the final result for one scale parameter value, the process depicted in Figure 3 outputs 100 classification results, with one at each scale parameter. This map provides a close-up of the result of the weighted overlay process, which outputs a raster referred to as Crater Score, which indicates the likelihood of a pixel being a crater.

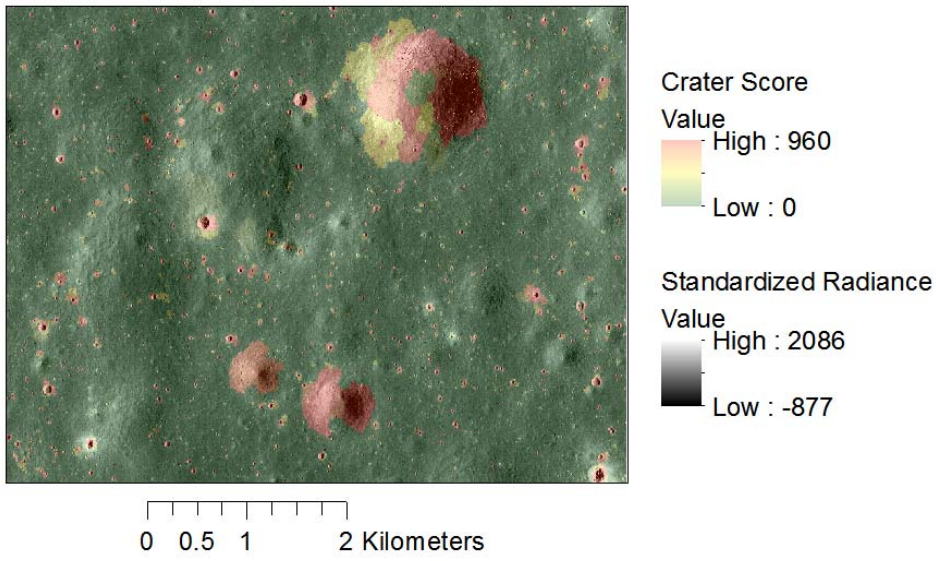

Figure 5: Accuracy Assessment Results.

4. Results

Although the CDA community lacks a standard method of assessing the quality of results (23), certain metrics frequently occur in the literature. In order to assess the quality of results, ground truth is necessary (1, 4, 28). Although some researchers utilize existing crater catalogs as ground truth, others create their own ground truth by manually identifying craters within their study area (4, 20, 37, 28). True detection rate (TDR) and false detection rate (FDR) are frequently used and can be calculated using true positive (TP), false negative (FN), and false positive (FP) as TDR=TP/(TP+FN) and FDR=FP/(TP+FP) (15, 1, 4, 20, 22, 38, 29, 23, 40). As TDR increases, so does FDR (20). Another frequently used metric is quality rate (QR), which describes overall performance and can be calculated as QR=TP/(TP+FP+FN) (15, 4, 38, 29, 40). When used alone, any of the above metrics can be misleading. Therefore, it is recommended to provide several accuracy metrics in order to assess multiple aspects of the result (7). TDR, FDR, and QR are all calculated for this study.

For accuracy assessment, craters with a radius less than 1.5 meters are not considered, even though the CDA does detect craters smaller than this. The upper bound in size is determined by the size of the image, since no mosaicking was done. However, if mosaicking were done, then the CDA would theoretically be capable of detecting larger craters. Any craters that are not mostly contained within the study area are not considered in the accuracy assessment. If a detected crater is over 1.5 times the size of the actual crater, then the excess portion is considered a false positive and the actual portion is considered a true positive. Each false positive is a contiguous area. While some false positives are spatially contiguous with true positives, other false positives are not. Regardless of whether they are the former or the latter case, they are each counted as one false positive. Any Crater Score above zero indicates a detected crater. If the majority of a crater is detected, it counts as a true positive. Otherwise, it counts as a false negative. True negatives are inherently uncountable.

Existing crater catalogs do not contain craters as small as the craters this CDA detects, and no other ground truth exists. Therefore, this study area's ground truth is established by manually picking craters in ArcMap (Table 5). All craters in the study area that conform to the above criteria are used, facilitating the determination of true positives, false positives, and false negatives. The quality rate is calculated to be 60.11%. The true detection rate is 68.88%, and the false detection rate is 17.48% (Table 6). This is a successful result for a new CDA, and the accuracy is similar to other studies that utilize DEMs (Table 1). Since the LROC NAC imagery provides information at a much higher resolution, this CDA is capable of detecting small, previously undetected craters. Therefore, this is an improvement on previous OBIA CDAs.

Table 5: Accuracy Assessment Count. Number of true positives, false negatives, and false positives in study area.

	Count
True Positive (TP)	1,558
False Negative (FN)	704
False Positive (FP)	330

Table 6: Accuracy Assessment Metrics. Quality rate, true detection rate, and false detection rate for study area.

	Equation	Value
Quality Rate (QR)	QR = TP / (TP + FP + FN)	60.11%
True Detection Rate (TDR)	TDR = TP / (TP + FN)	68.88%
False Detection Rate (FDR)	FDR = FP / (TP + FP)	17.48%

5. Conclusion

This study uses object-based image analysis in ArcMap, eCognition, and Python to create a crater detection algorithm applied to the Moon. A novel technique is developed, utilizing the distinctive appearance of adjacent light and dark crescents to identify craters. The iteration of this technique over multiple scale parameters facilitates the detection of a range of crater sizes from roughly one meter to one kilometer. The quality rating of 60.11% is comparable to other results in the literature (Table 1), but this project makes a significant step forward by pioneering this method for high-resolution imagery.

Future work could focus on optimizing the weights associated with each scale parameter used in the weighted overlay step. It could also utilize mosaicking to extend the algorithm to detect craters larger than the size of the input images. More localized image standardization would eliminate many of the false positives present due to soil heterogeneity. Each of these refinements would improve the performance of this CDA. As high-resolution imagery becomes available on other lunar and planetary bodies, this technique could be applied. With these refinements to performance and additional applications, a further step could be taken towards achieving a universal CDA.

6. References

1. Bandeira, L., J. Saraiva, and P. Pina, 2007: Impact Crater Recognition on Mars Based on a Probability Volume Created by Template Matching. *IEEE Transactions on Geoscience and Remote Sensing*, **45(12)**, 4008-4015.
2. Bandeira, L., W. Ding, and T. F. Stepinski, 2012: Detection of sub-kilometer craters in high resolution planetary images using shape and texture features. *Advances in Space Research*, **49**, 64-74.
3. Bertani, T. C., D. F. Rossetti, and P. C. G. Albuquerque, 2013: Object-based classification of vegetation and terrain topography in Southwestern Amazonia (Brazil) as a tool for detecting ancient fluvial geomorphic features. *Computers and Geosciences*, **60**, 41-50.
4. Bue, B. D. and T. F. Stepinski, 2007: Machine Detection of Martian Impact Craters From Digital Topography Data. *IEEE Transactions on Geoscience and Remote Sensing*, **45(1)**, 265-274.
5. Bujan, S., E. Gonzalez-Ferreiro, F. Reyes-Bueno, L. Barreiro-Fernandez, R. Crecente, and D. Miranda, 2012: Land Use Classification from Lidar Data and Ortho-Images in a Rural Area. *The Photogrammetric Record*, **27(140)**, 401-422.
6. Burl, M. C. and P. G. Wetzler, 2011: Onboard object recognition for planetary exploration. *Machine Learning*, **84**, 341-367.
7. Cohen, J. P. and W. Ding, 2014: Crater detection via genetic search methods to reduce image features. *Advances in Space Research*, **53**, 1768-1782.
8. De Pater, I. and J. J. Lissauer, 2011: Planetary Sciences. *Cambridge University Press*, Second Edition.
9. Ding, W., T. F. Stepinski, Y. Mu, L. Bandeira, R. Ricardo, Y. Wu, Z. Lu, T. Cao, and X. Wu, 2011: Subkilometer Crater Discovery with Boosting and Transfer Learning. *ACM Transactions on Intelligent Systems and Technology*, **2(4)**, 1-22.

10. Ghosh, S., T. F. Stepinski, and R. Vilalta, 2010: Automatic Annotation of Planetary Surfaces With Geomorphic Labels. *IEEE Transactions on Geoscience and Remote Sensing*, **48(1)**, 175-185.
11. Head, J. W., C. I. Fassett, S. J. Kadish, D. E. Smith, M. T. Zuber, G. A. Neumann, and E. Mazarico, 2010: Global Distribution of Large Lunar Craters: Implications for Resurfacing and Impactor Populations. *Science*, **329**, 1504-1507.
12. Jin, S. and T. Zhang, 2014: Automatic detection of impact craters on Mars using a modified adaboosting method. *Planetary and Space Science*, **99**, 112-117.
13. Kadish, S. J., C. I. Fassett, J. W. Head, D. E. Smith, M. T. Zuber, G. A. Neumann, and E. Mazarico, 2011: A Global Catalog of Large Lunar Craters (≥20 km) from the Lunar Orbiter Laser Altimeter. *42nd Lunar and Planetary Science Conference*, 1006-1007.
14. Ke, Y., L. J. Quackenbush, and J. Im, 2010: Synergistic use of QuickBird multispectral imagery and LIDAR data for object-based forest species classification. *Remote Sensing of Environment*, **114**, 1141-1154.
15. Kim, J. R., J. P. Muller, S. V. Gasselt, J. G. Morley, and G. Neukum, 2005: Automated Crater Detection, A New Tool for Mars Cartography and Chronology. *Photogrammetric Engineering and Remote Sensing*, **71(10)**, 1205-1217.
16. "Lunar Reconnaissance Orbiter." National Aeronautics and Space Administration – Goddard Space Flight Center. http://lro.gsfc.nasa.gov/index.html. (accessed December 10, 2014).
17. Luo, L., L. Mu, X. Wang, C. Li, W. Ji, J. Zhao, and H. Cai, 2013: Global detection of large lunar craters based on the CE-1 digital elevation model. *Frontiers in Earth Science*, **7(4)**, 456-464.
18. Martha, T. R., N. Kerle, V. Jetten, C. J. V. Westen, and K. V. Kumar, 2010: Characterizing spectral, spatial and morphometric properties of landslides for semi-automatic detection using object-oriented methods. *Geomorphology*, **116**, 24-36.

19. Martha, T. R., N. Kerle, C. J. V. Westen, V. Jetten, and K. V. Kumar, 2012: Object-oriented analysis of multi-temporal panchromatic images for creation of historical landslide inventories. *ISPRS Journal of Photogrammetry and Remote Sensing*, **67**, 105-119.
20. Martins, R., P. Pina, J. S. Marques, and M. Silveira, 2009: Crater Detection by a Boosting Approach. *IEEE Geoscience and Remote Sensing Letters*, **6(1)**, 127-131.
21. Mehta, A., O. Dikshit, and K. Venkataramani, 2014: Integration of high-resolution imagery and LiDAR data for object-based classification of urban area. *Geocarto International*, **29(4)**, 418-432.
22. Meng, D., C. Yunfeng, and W. Qingxian, 2009: Method of Passive Image Based Crater Autonomous Detection. *Chinese Journal of Aeronautics*, **22**, 301-306.
23. Meng, D., C. Yunfeng, and W. Qingxian, 2013: Novel approach of crater detection by crater candidate region selection and matrix-pattern-oriented least squares support vector machine. *Chinese Journal of Aeronautics*, **26(2)**, 385-393.
24. Mullerova, J., J. Pergl, and P. Pysek, 2013: Remote sensing as a tool for monitoring plant invasions: Testing the effects of data resolution and image classification approach on the detection of a model plant species *Heracleum mantegazzianum* (giant hogweed). *International Journal of Applied Earth Observation and Geoinformation*, **25**, 55-65.
25. Rosa, M. F. and D. A. Stow, 2014: Mapping fuels at the wildland-urban interface using color ortho-images and LiDAR data. *Geocarto International*, **29(5)**, 570-588.
26. Salamuniccar, G. and S. Loncaric, 2008: Open framework for objective evaluation of crater detection algorithms with first test-field subsystem based on MOLA data. *Advances in Space Research*, **42**, 6-19.

27. Salamuniccar, G. and S. Loncaric, 2008: GT-57633 catalogue of Martian impact craters developed for evaluation of crater detection algorithms. *Planetary and Space Science*, **56**, 1992-2008.

28. Salamuniccar, G. and S. Loncaric, 2010: Method for Crater Detection From Martian Digital Topography Data Using Gradient Value/Orientation, Morphometry, Vote Analysis, Slip Tuning, and Calibration. *IEEE Transactions on Geoscience and Remote Sensing*, **48(5)**, 2317-2329.

29. Salamuniccar, G., S. Loncaric, P. Pina, L. Bandeira, and J. Saraiva, 2011: MA130301GT catalogue of Martian impact craters and advanced evaluation of crater detection algorithms using diverse topography and image datasets. *Planetary and Space Science*, **59**, 111-131.

30. Salamuniccar, G., S. Loncaric, D. Vinkovic, D. Vucina, M. Gomercic, I. Pehnec, M. Vojkovic, and T. Hercigonja, 2012: Test-field for evaluation of laboratory craters using a Crater Shape-based interpolation crater detection algorithm and comparison with Martian and Lunar impact craters. *Planetary and Space Science*, **71**, 106-118.

31. Salamuniccar, G. and S. Loncaric, 2012: Crater detection algorithms: a survey of the first decade of intensive research. *Horizons in Earth Science Research*, **8**, 93-123.

32. Salamuniccar, G., S. Loncaric, A. Grumpe, and C. Wohler, 2014: Hybrid method for crater detection based on topography reconstruction from optical images and the new LU78287GT catalogue of Lunar impact craters. *Advances in Space Research*, **53**, 1783-1797.

33. Salehi, B., Y. Zhang, M. Zhong, and V. Dey, 2012: Object-Based Classification of Urban Areas Using VHR Imagery and Height Points Ancillary Data. *Remote Sensing*, **4**, 2256-2276.

34. Sasaki, T., J. Imanishi, K. Ioki, Y. Morimoto, and K. Kitada, 2012: Object-based classification of land cover and tree species by integrating airborne LiDAR and high spatial resolution imagery data. *Landscape and Ecological Engineering*, **8**, 157-171.

35. Sawabe, Y., T. Matsunaga, and S. Rokugawa, 2006: Automated detection and classification of lunar craters using multiple approaches. *Advances in Space Research*, **37**, 21-27.

36. Smith, D. E., M. T. Zuber, G. A. Neumann, F. G. Lemoine, E. Mazarico, M. H. Torrence, J. F. McGarry, D. D. Rowlands, J. W. Head, T. H. Duxbury, O. Aharonson, P. G. Lucey, M. S. Robinson, O. S. Barnouin, J. F. Cavanaugh, X. Sun, P. Liiva, D. Mao, J. C. Smith, and A. E. Bartels, 2010: Initial observations from the Lunar Orbiter Laser Altimeter (LOLA). *Geophysical Research Letters*, **37**, 18204-18209.

37. Stepinski, T. F., M. P. Mendenhall, and B. D. Bue, 2009: Machine cataloging of impact craters on Mars. *Icarus*, **203**, 77-87.

38. Urbach, E. R. and T. F. Stepinski, 2009: Automatic detection of sub-km craters in high resolution planetary images. *Planetary and Space Science*, **57**, 880-887.

39. Veljanovski, T., U. Kanjir, and K. Ostir, 2011: Object-Based Image Analysis of Remote Sensing Data. *Geodetski vestnik*, **55(4)**, 665-688.

40. Vijayan, S., K. Vani, and S. Sanjeevi, 2013: Crater detection, classification and contextual information extraction in lunar images using a novel algorithm. *Icarus*, **226**, 798-815.

41. Wan, C., W. M. Cheng, Z. P. Zhou, S. M. Zhao, and Y. Xia, 2012: Automatic extraction of lunar impact craters from Chang'E-1 satellite photographs. *Science China – Physics, Mechanics and Astronomy*, **55(1)**, 162-169.

42. Westfall, J. E., 2000: Atlas of the Lunar Terminator. *Cambridge University Press*, 30-43.

43. Yue, Z. Y, J. Z. Liu, and G. G. Wu, 2008: Automated detection of lunar craters based on object-oriented approach. *Chinese Science Bulletin*, **53(23)**, 3699-3704.

44. Zhang, D., C. Zhang, R. Cromley, D. Travis, and D. Civco, 2012: An Object-Based Method for Contrail Detection in AVHRR Satellite Images. *GIScience and Remote Sensing*, **49(3)**, 412-427.

45. Ziaei, Z., B. Pradhan, and S. B. Mansor, 2013: A rule-based parameter aided with object-based classification approach for extraction of building and roads from WorldView-2 images. *Geocarto International*, **29(5)**, 554-569.